A Sub-5mW Monolithic CMOS-MEMS Thermal Flow Sensing SoC With ±6 m/s Linear Range

Wei Xu, *Senior Member, IEEE*, Zhijuan Li, Zetao Fang, Bo Wang, *Senior Member, IEEE*, Linze Hong, Gai Yang, Su-Ting Han, Xiaojin Zhao, *Senior Member, IEEE*, and Xiaoyi Wang, *Member, IEEE*

***Abstract*— This article presents a complementary metal-oxide semiconductor (CMOS)-microelectromechanical system (MEMS) monolithic integrated thermal flow sensor system, which consists of a MEMS sensor with dual pairs of thermistors, a precise constant temperature difference (CTD) control circuit, and a low-noise readout circuit with a current feedback instrument amplifier (CFIA). The MEMS sensor is fabricated using an in-house developed post-CMOS process, while its sensing structure is thinned to 2.52 μm for power reduction. Meanwhile, the distance between the microheater and thermistors is optimized with a linear range of larger than ±4 m/s by the Peclet number (Pe) <1 criterion. The designed CTD control circuit can offer a driving current of 1.88 mA with an output swing of up to 2.82 V, which enables the microheater to operate in 50-K CTD mode with a deviation of less than 0.01 K. Additionally, the designed CFIA has a noise floor of 12.4 nV/rtHz with a 1/f corner of less than 400 mHz. The performance of the system-on-chip (SoC) sensor is evaluated with N_2 gas flow. The SoC sensor has a high sensitivity of 156 mV/(m/s) with a detectable flow range of up to ±11 m/s, while its system power is less than 5 mW. The SoC sensor also has state-of-the-art linearity in a range of ±6 m/s and a detection limit down to 86 μm/s. Moreover, the tested results of this SoC sensor are in good agreement with the theoretical models, confirming the feasibility of the proposed design strategy.**

***Index Terms*— CMOS interface, complementary metal-oxide semiconductor (CMOS)-microelectromechanical system (MEMS) monolithic integration, gas flow, linear range, low power, MEMS, thermal flow sensor.**

Manuscript received 20 April 2023; revised 17 June 2023 and 13 August 2023; accepted 10 September 2023. Date of publication 22 September 2023; date of current version 25 April 2024. This article was approved by Associate Editor Piero Malcovati. This work was supported in part by the National Natural Science Foundation of China under Grant 52105582, in part by the Natural Science Foundation of Guangdong Province under Grant 2022A1515010894, in part by the Shenzhen Science and Technology Program under Grant JCYJ20210324095210030, Grant JCYJ20220818095810023, and Grant ZDSYS20220527171402005, in part by the Shenzhen-Hong Kong-Macau S&T Program (Category C) under Grant SGDX20210823103200004, and in part by the Beijing Institute of Technology Research Fund Program for Young Scholars under Grant XSQD-202206004. *(Corresponding authors: Xiaoyi Wang; Xiaojin Zhao.)*

Wei Xu, Zhijuan Li, Zetao Fang, Linze Hong, Su-Ting Han, and Xiaojin Zhao are with the State Key Laboratory of Radio Frequency Heterogeneous Integration and the College of Electronics and Information Engineering, Shenzhen University, Shenzhen 518060, China (e-mail: weixu@szu.edu.cn; eexjzhao@szu.edu.cn).

Bo Wang is with the College of Science and Engineering, Hamad Bin Khalifa University, Doha, Qatar (e-mail: bwang@hbku.edu.qa).

Gai Yang and Xiaoyi Wang are with the School of Integrated Circuits and Electronics, Beijing Institute of Technology, Beijing 100081, China (e-mail: xiaoyiwang@bit.edu.cn).

Color versions of one or more figures in this article are available at https://doi.org/10.1109/JSSC.2023.3314765.

Digital Object Identifier 10.1109/JSSC.2023.3314765

I. Introduction

FLOW measurement has been an essential requirement in many biomedical and industrial applications [1], [2], one of the urgent needs is low-cost and high-performance flow sensors for respiratory monitoring [3], [4]. Typically, during normal breathing, the maximum airflow velocity through the nose in humans is approximately 4 m/s [5]. Consequently, flow sensors connected to breathing tubes must be capable of detecting low airflow velocities below 4 m/s or even below 0.1 m/s to identify high-risk situations such as hypopnea or apnea [6], [7]. Conventional flow measurement instruments were bulky, expensive, and interfered with the flow, making them unsuitable for low-cost and highly accurate low-flow measurements in biomedical applications. Benefit from the microelectromechanical systems (MEMS) technology, flow sensors with low power and small size designs could be realized [8], [9], [10]. To date, many research efforts on microflow sensors have been carried out, and significant progress has been made in their alternative transduction principles [11], performance improvements [12], [13], microfabrication techniques [14], packaging and testing methods [15], [16], and many others.

According to the sensing principle, these miniaturized flow sensors can be categorized as hot wire/hot film [17], calorimetric [18], cantilever [19], Karman vortex [20], Coriolis [21], bionic [22], and so on. The cantilever, vortex, and coriolis flow sensors, also known as nonthermal flow sensors, mainly rely on sensing microstructure deformation or fluid vortex shedding for flow measurement [19], [21], [22]. However, their capability to measure low flow is limited, as the fluid does not undergo vortex shedding or produce prominent microstructural deformation at the low Reynolds number (Re) flow, rendering them unsuitable for accurate respiration measurements. The hot wire/hot film sensor detects flow by measuring heat loss from a heating element in the fluid. Although it has a simple structure, it cannot measure the flow direction, and the interference of natural convection limits its measurement accuracy at low flow [23]. Recently, bio-inspired sensors have achieved impressive progress in detecting extremely low gas flow below 0.05 m/s [22], [24]. However, due to issues such as sensing structure reliability and complementary metal-oxide semiconductor (CMOS) compatibility, they are difficult to achieve low-cost large-scale fabrication and reliable long-term measurement, which makes their application in "harsh" breathing environments challenging.

On the other hand, calorimetric flow sensor realizes flow measurement by monitoring the flow-induced asymmetric temperature distribution around a microheater [25], [26], and the flow direction can be determined by using multiple temperature-sensitive elements [27], [28]. The symmetrical arrangement of the sensitive elements ensures that the temperature difference between upstream and downstream solely reflects heat convection, resulting in improved sensitivity and accuracy, particularly in low flow [29]. Furthermore, microcalorimetric flow sensors do not require any movable micromechanical parts, which makes them perhaps the easiest flow devices to be implemented in the CMOS process due to their structural and electronic simplicity.

By leveraging mature CMOS or CMOS-MEMS techniques, MEMS flow sensors combined with integrated circuits (ICs) can be carried out, which can easily enable a miniaturized sensor system with better performance [30], [31], [32], while reducing packaging costs and shortening the development cycle [33]. The research of CMOS-MEMS integrated calorimetric flow sensors has therefore gained significant interest [34], [35], [36], [37], [38], [39]. For example, Brevet et al. [37] proposed a monolithically integrated CMOS thermal wind sensor with a chip size of 4 × 4 mm^2; however, the microheater and sensitive elements were fabricated directly on the silicon substrate, which results in high power consumption. Recently, De Luca and Udrea [38] proposed an integrated flow sensor utilizing an SOI CMOS-MEMS process, which features a suspended circular membrane with a heating power of 13 mW. Despite the low power sensor design, its sensitivity enhancement is constrained by a relatively thick film structure (~5 μm), impeding it from achieving accurate gas flow measurements below 0.05 m/s, while such an approached mm/s level low flow measurement capability is critical for the respiratory application.

As evident from [29], low flow measurement can be realized with a highly sensitive MEMS design while minimizing electronic and mechanical noise from the interface circuit and thermally-induced gas fluctuations, respectively. To facilitate this, an effective approach is to develop a microstructure with high sensitivity and a low-noise circuit interface, while keeping the system power budget minimal (several mW level for extended battery life). Unfortunately, the thickness of the back-end-of-line (BEOL) layers (>10 μm for 0.18 μm technology node) in CMOS still presents a challenge for enhancing sensor sensitivity and reducing power consumption [40], [41]. In addition, achieving linearity is also a critical design objective for flow sensors. While calorimetric flow sensors have shown a linear response at low flow [42], these sensors cannot deliver a linear response with high sensitivity over a range larger than ±4 m/s, to the best of our knowledge. Consequently, considerable effort and time are still required for nonlinear sensor response calibration in respiratory monitoring, which in turn drives up the sensor cost. Therefore, it is essential to develop a low-cost CMOS-MEMS integrated flow sensor system with a high sensitivity, wide linear range, and low-power consumption for low gas flow in respiratory applications.

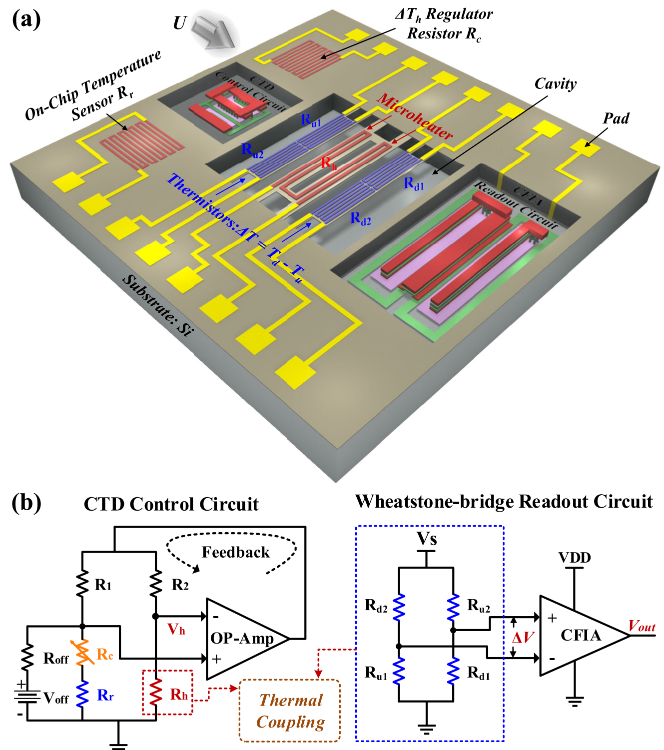

Fig. 1. (a) Schematic of a monolithically integrated SoC thermal flow sensor system with dual pairs of thermistors using a 0.18 μm CMOS-MEMS technology. (b) Interface circuit for the MEMS sensor: (left) CTD control circuit; (right) Wheatstone bridge readout circuit with CFIA.

In this article, we proposed a CMOS-MEMS monolithic integrated thermal flow sensor system with a chip size of only around 2.5 × 1.5 mm. The delicately designed system on chip (SoC) sensor is composed of a MEMS sensor with dual pairs of thermistors for sensitivity improvement, a precise constant temperature difference (CTD) control circuit, and a low-noise readout circuit with current feedback instrument amplifier (CFIA). Testing results show that the SoC sensor has a high sensitivity of 156 mV/(m/s) with a system power of less than 5 mW, while achieving a wide linear range of ±6 m/s and low flow measured down to 86 μm/s. The rest of this article is organized as follows. Section II details the sensor system and design considerations for MEMS sensor and CMOS interface circuit. Section III briefly presents the fabrication of the proposed SoC sensor. In Section IV, measurement results are discussed and compared with other state-of-the-art flow sensors. Finally, Section V concludes this article.

II. Sensor System and Design Considerations

A. Proposed SoC Sensor System

The proposed monolithic integrated thermal flow sensor system is depicted in Fig. 1(a), it comprises a MEMS structure with dual pairs of thermistors, a precise CTD control circuit, and a low-noise CFIA readout circuit. Among them, the 2.52 μm thick MEMS structure will be released by a home-developed post-CMOS process, and a bottom cavity in silicon substrate will be formed for sensor power reduction. Note that the entire sensor system is designed and implemented on a single chip using 0.18 μm CMOS-MEMS technology.

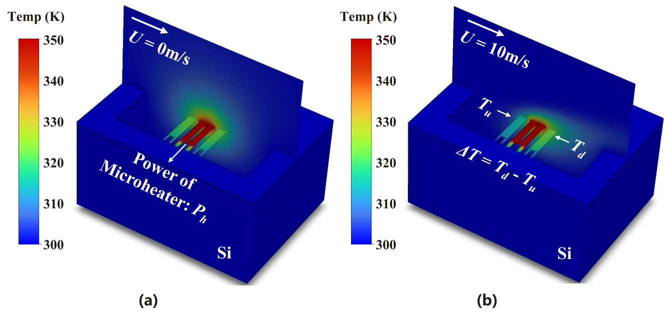

Fig. 2. Temperature profile around split microheater in 3-D CFD simulation (a) with and (b) without gas flow. Note the microbridges are simplified as pure oxide structures to save the calculation time, and the microheater works on a 50 K CTD mode with an ambient temperature of 300 K.

During the operation of the SoC sensor system, the microheater R_h, placed in the central microbridge, maintains a CTD with respect to the ambient through a CTD control circuit, as shown in the left part of Fig. 1(b). When in the absence of fluid flow, the temperature distribution around R_h is symmetrical, as proved by a 3-D computational fluid dynamics (CFDs) simulation shown in Fig. 2(a). While in the presence of fluid flow U, the temperature distribution around R_h is distorted, causing a temperature difference output of $\Delta T = T_d - T_u$ through heat transfer, as shown in Fig. 2(b). The thermal output ΔT can be converted into an electrical signal ΔV through a Wheatstone bridge formed by upstream and downstream thermistors R_{u1} & R_{u2} and R_{d1} & R_{d2}, as shown in the right portion of Fig. 1(b). The signal of ΔV is then amplified using a low-noise CFIA. Thus, the final output of the sensor system, V_{out}, can be related to the input flow U, as follows:

$$V_{\text{out}} \approx 0.5\alpha V_s G \Delta T \tag{1}$$

where V_s is the applied voltage in the Wheatstone bridge, G is the gain of signal amplification, and α is the temperature coefficient of resistance (TCR) of ploy-Si. From (1), one can improve the flow measurement accuracy by increasing the sensor output and lowering the system noise, i.e., signal-to-noise ratio. This can be achieved by using high TCR thermistors while designing a low-noise interface circuit. Besides, to improve the thermal output ΔT within a limited heating power budget (<mW level), a dual pair of thermistors with a reduced film thickness of 2.52 μm is preferred in this article, which provides a doubled sensor output as compared to the single pair design [26].

B. Design of MEMS Flow Sensor

In the detailed MEMS sensor design, the 0.2 μm thick P+ polysilicon layer is adopted to form the microheater R_h, four thermistors, and the on-chip temperature sensor R_r, considering its good TCR of 2.91 $\times$ 10^{-3}/K when referring to a temperature of 25 °C, while the aluminum layer is used as lead wires. The microheater comprises a split microstructure with a 5 μm gap, and its serpentine layout is formed by a 4 μm wide wire. The designed microheater has a heating area of 126 $\times$ 28 μm and an average resistance of 1019 Ω measured at 25 °C. This is done to increase the affordable power of the microheater and prevent damage to the polysilicon film during joule heating. Two pairs of upstream and downstream thermistors are also designed with the same layout patterns, each covering an area of 67 $\times$ 15 μm. To minimize the self-heating issue, each thermistor is designed as a serpentine structure formed by a 1 μm wide wire, and their average resistance is relatively larger than that of the microheater, which is 4056 Ω at 25 °C. Additionally, to achieve a CTD between the microheater and the ambient, a temperature sensor R_r is integrated on the silicon substrate for automatic regulation of the heating temperature [43], [44].

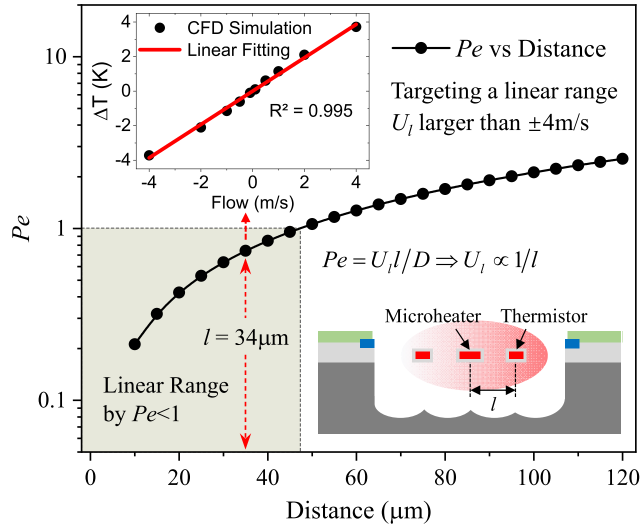

Fig. 3. Linear range of the SoC sensor system is designed to be larger than ±4 m/s based on the Peclet number (Pe) criterion. Accordingly, the distance l between the microheater and the temperature sensor is designed as 34 μm with $Pe < 1$.

To further optimize the distance between the microheater and thermistors, the Peclet number (Pe) ≤ 1 criterion that determines the linear range of a calorimetric flow sensor is used [45]. As illustrated in (2), the linear range of the flow sensor U_l is inversely proportional to the distance l between the microheater and thermistors

$$Pe = U_l l / D \tag{2}$$

where D is the thermal diffusivity.

In Fig. 3, the calculated Pe is plotted as a function of the distance l, while the thermal diffusivity D is determined by the averaged thermal properties of air and microbridges. To achieve a linear range larger than ±4 m/s, a distance of $l < 47$ μm is suggested by $Pe < 1$. Note that when $Pe < 1$, it indicates a weak thermal convection and a dominant thermal diffusion, which corresponds to the case of the thermal perturbation analysis for the linear low flow discussed in [42]. This conclusion is also confirmed by the linear fit of the CFD results, with good linearity obtained ($R^2 > 0.995$) in the flow range of ±4 m/s. In consideration of the adopted SMIC 0.18 μm 1P6M CMOS process and the in-house developed post-CMOS process, the distance l between the microheater and the thermistors is designed as 34 μm. In this case, Pe is equal to 0.72, and we may expect a wider linear range than

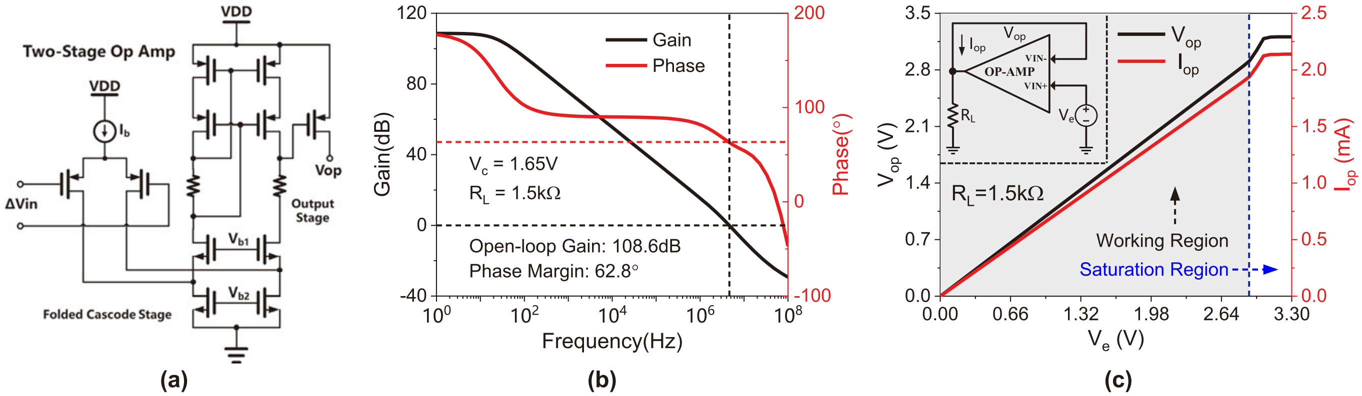

Fig. 4. (a) Block diagram of the implemented folded-cascode amplifier with a PMOS buffer. (b) Open-loop gain and phase of the designed CTD control circuit are 108.6 dB and 62.8°, respectively. (c) With a load of 1.5 kΩ, the output swing and current drive capability of the op-amp designed for the CTD control circuit are 2.9 V and 1.93 mA, respectively.

the design target when considering the heat conduction losses from the ends of the microbridges.

C. Design of CMOS Interface Circuit

Interface circuitry is also implemented on the CMOS die (Fig. 1) to realize a tangible SoC flow sensor solution, including a precise CTD control circuit and a low-noise readout circuit.

1) CTD Circuit: The main purpose of designing this CTD circuit is to improve the temperature drift compensation capability of the microcalorimetric flow sensor [44]. The CTD circuit comprises several components, including microheater R_h, on-chip ambient temperature sensor R_r, regulating resistor R_c, poly-Si resistors R_1 & R_2, and an operational amplifier. When fluid flows over the microheater, its resistance decreases due to the cooling effect, resulting in an increased voltage difference at the input ends of the operational amplifier. Consequently, an elevated voltage is fed into the Wheatstone bridge, causing an increase in heating power, which increases the resistance of the microheater and rebalance the Wheatstone bridge. When the CTD circuit is functioning properly, the overheated temperature ΔT_h of the microheater can be simply regulated by the resistor R_c and maintained at a constant value, as shown below

$$\Delta T_h = T_h - T_a = R_c \big/ \alpha R_r(T_0) \tag{3}$$

where T_a is the ambient temperature and $R_r(T_0)$ is the resistance of the ambient temperature sensor R_r at the reference temperature of T_0.

As per the operating principle of the CTD circuit, more sensor power is needed to maintain a constant ΔT_h when fluid flow increases. To target this goal, it is recommended that the amplifier utilized in the CTD circuit possess an open-loop gain exceeding 80 dB. Such a configuration would yield a maximum unbalanced voltage of approximately 0.33 mV within a 3.3 V system. This discrepancy, when compared to the ideal scenario with infinite gain, would only result in a worst case ΔT_h drop of less than 0.07% for microheater voltages close to 1 V, even under different flow conditions. Meanwhile, as proved by CFD simulation, the power loss of the microheater, which works in a 50 K CTD mode, remains below 1 mW within an input flow of 0–10 m/s. Considering the nominal design of R_h around 1 kΩ and a bridge ratio of $R_1/R_2 = 5{:}1$ (ensures that most of the CTD circuit power is consumed by the microheater), it is imperative that the amplifier should be capable of supplying a minimum driving current of 1.2 mA to the Wheatstone bridge.

In this article, a folded-cascode amplifier incorporating a PMOS buffer with a strong current driving capability is devised, as shown in Fig. 4(a). Note that the designed folded cascode stage consumes a power of 0.13 mW with a 3.3 V supply. The simulation result, illustrated in Fig. 4(b), shows that the designed operational amplifier has an open-loop gain of 108.6 dB and a phase margin of 62.8°. Therefore, it can be inferred that the designed operational amplifier is deemed to be stable. Utilizing a 400 μm (W) × 340 nm (L) PMOS buffer, the output swing and current drive capability of the operational amplifier are simulated as 2.9 V and 1.93 mA, respectively, when subjected to a load of 1.5 kΩ, as shown in Fig. 4(c). To ensure that the CTD circuit operates within the working region (<2.9 V) rather than the saturation region, the ratio of R_2/R_h is designed as 1:2, as suggested by

$$\frac{R_2}{R_h} > \frac{\left|V_{\text{th,pmos}}\right|}{V_{\text{DD}} - \left|V_{\text{th,pmos}}\right|} \tag{4}$$

where V_{DD} is equal to 3.3 V and $V_{\text{th,pmos}}$ is the threshold voltage of the PMOS in the folded cascode differential input pair, which is −589 mV in this design. With this configuration, the designed CTD circuit can deliver a maximum of 3.11 mW to the microheater. Therefore, the proposed interface circuit can make sure the microheater works well in a 50 K CTD mode, as the CFD simulation proves that its required power is <1 mW.

2) CFIA Readout Circuit: Since the voltage output ΔV of the Wheatstone bridge is typically in mV level or even lower at low flow conditions, it becomes necessary to amplify the sensor signal for subsequent signal processing. Considering that the thermal noise floor of the Wheatstone bridge is around 8.2 nV/$\sqrt{\text{Hz}}$, the targeted noise floor of the designed amplifier is selected as the same level, i.e., 8 nV/$\sqrt{\text{Hz}}$, for a low-power

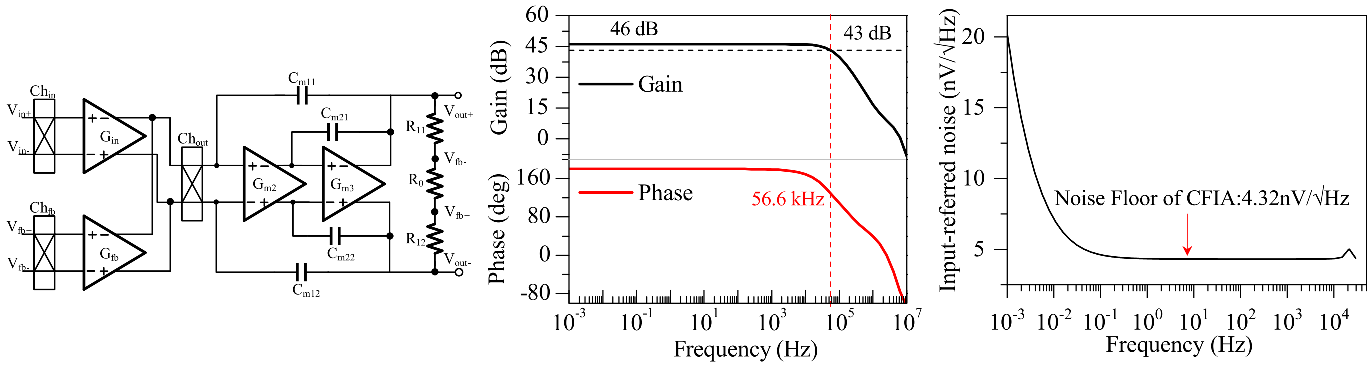

Fig. 5. (a) Block diagram of implemented chopped CFIA. (b) Frequency response simulation result with a closed-loop gain of 200. Note that the bandwidth when the closed-loop gain decreases by 3 dB is 56.6 kHz. (c) Simulated input-referred noise spectrum showing the thermal noise floor is around 4.32 nV/$\sqrt{}$Hz, and the flicker corner is around 400 mHz. Note that there is a spike near the chopping frequency due to the use of chopping modulation technology.

design purpose. Furthermore, when a closed-loop gain of 200 with a gain error of less than 0.1% is required, the loop gain should be greater than 1000. Therefore, the minimum open-loop gain of the amplifier should be larger than 106 dB.

According to the above requirements, a low-noise CFIA is designed as the analog front-end due to its high CMRR [46] and large input impedance [47]. The chopped CFIA is implemented with a three-stage topology, as shown in Fig. 5(a). Compared with the two-stage topology, the three-stage CFIA can achieve an open-loop gain greater than 150 dB, which can effectively suppress the closed-loop gain error and improve CMRR [48]. In this particular design, the input transconductance $g_{m,in}$ and feedback transconductance $g_{m,fb}$ are chopped to minimize offset and flicker noise, while the second- and third-stage amplifiers are designed with very high dc gain. Among them, the last stage is implemented using a class AB push-pull amplifier while maintaining power efficiency and good driving capability. Upon implementation of a three-stage topology in CFIA, three poles are exhibited, leading to concerns regarding circuit stability. To address this issue, the utilization of nested miller compensation (NMC) is recommended, which simply requires capacitors for improved circuit stability [49]. Note that the NMC incorporates local Miller capacitors, namely C_{m21} and C_{m22}, situated around the final stage of CFIA, along with global Miller feedback capacitors of C_{m11} and C_{m12}. Additionally, the feedback compensation capacitors (C_{m21} and C_{m22}) in class AB help to filter out the ripple at the chopper frequency, while any remaining ripple can be further eliminated using an external RC filter. To minimize the gain error of the CFIA, the input and feedback transconductance are designed to be identical, i.e., $g_{m,in} = g_{m,fb}$. In this case, the closed-loop gain of CFIA is exactly given by the following equation:

$$Gain = \left(\frac{R_{11} + R_0 + R_{12}}{R_0}\right). \quad (5)$$

Fig. 5(b) shows the simulated frequency response of the CFIA when its closed-loop gain is set to 200 (46 dB). The CFIA exhibits a bandwidth of 56.6 kHz. This specific bandwidth design enables the implementation of a 20 kHz chopping frequency to reduce the corner frequency of the flicker noise. Besides, additional simulations confirm that the CFIA is conditionally stable for a closed-loop gain greater than 50. Fig. 5(c) shows the simulated noise spectral density (NSD) of the chopped CFIA, where the flicker noise corner is less than 400 mHz and the thermal noise floor is around 4.32 nV/$\sqrt{}$Hz, which is lower than the target value of 8 nV/$\sqrt{}$Hz. Such a designed low-noise amplifier (CFIA) can serve as a good interface readout circuit for the SoC flow sensor.

D. SoC Sensor Performance

Generally, the design based on the thermal and fluid dynamic simulations is unable to take into transduction process of mechanical, thermal, and electrical domains that altogether contribute to the overall sensor performance. To have a more comprehensive performance evaluation of a proposed SoC flow sensor, system-level modeling and analysis are needed. Previously, we have introduced two important equivalent circuit models (ECMs) for the microheater in the CTD circuit, and the thermistors in the Wheatstone bridge-based readout circuit [44], and these two ECMs were thermally coupled with MEMS structure through an analytical model [25]. Based on the proposed system-level model [44], the entire CMOS-MEMS sensor system is built on the Cadence Virtuoso platform, and the system-level simulation and performance evaluation of the designed SoC flow sensor is realized.

As displayed in Fig. 6(a), the overheated temperature ΔT_h of the microheater, simulated by the system-level model, remains almost constant at 50 °C, and its variation is less than 0.01 °C at different input flow velocities. In addition, the power of the microheater is less than 0.89 mW. Therefore, the designed interface circuit can ensure that the microheater works in the CTD mode without being affected by the cooling effect of fluid flow. Fig. 6(b) shows the simulated sensor output and its comparison with the CFD model. Within the flow range of 0–10 m/s, the system-level model predicted output is in good agreement with the output from the CFD model. Besides, the SoC sensor has a high sensitivity of 148 mV/(m/s) in a linear flow range of 0–4 m/s. As proved by the system-level simulation in EDA, the proposed CMOS-MEMS monolithic

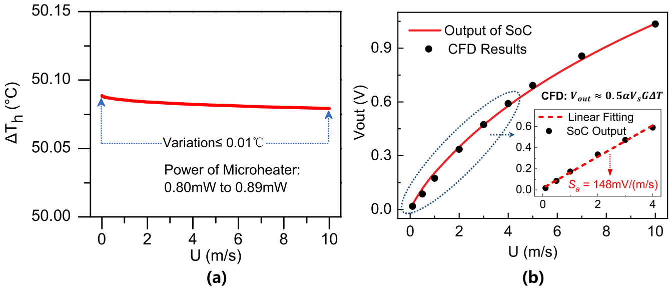

Fig. 6. (a) System-level model shows that the temperature difference between the microheater and the ambient is well controlled at $\Delta T_h = 50$ °C with a variation of less than 0.01 °C, and the heating power is less than 0.89 mW. (b) Comparison of SoC sensor output between the system-level model and CFD model ($V_s \times G = 100$), where the designed SoC sensor has a high sensitivity of 148 mV/(m/s) in a linear flow range of 0–4 m/s.

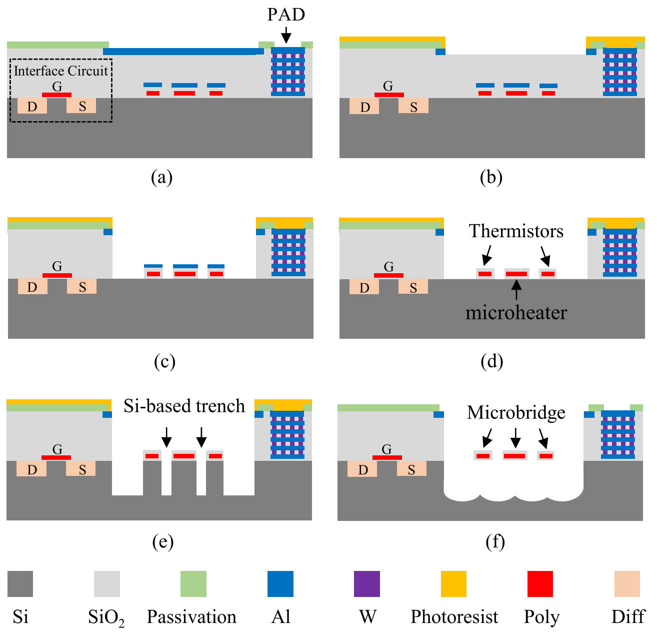

Fig. 7. In-house developed post-CMOS fabrication steps for the release of the SoC flow sensor. (a) Chip prepared by CMOS. (b) Photolithography and dry etching of aluminum. (c) RIE oxide etching. (d) Dry etching of aluminum. (e) Trench Structure by DRIE. (f) XeF_2 releasing and PR removing.

integrated thermal flow sensor system can detect gas flow up to 10 m/s with a system power at the mW level.

III. Fabrication of SoC Sensor

Fig. 7 illustrates the in-house developed post-CMOS process for the microfabrication of the SoC flow sensor. First, the sensor chip (2.5 × 1.5 mm) prepared by the SMIC 1P6M CMOS process was glued on a 4-inch Si wafer with the coated photoresist. Second, a 4 μm thick AZ9260 photoresist was spray coated on the sensor surface. Subsequently, as shown in Fig. 7(b), photolithography was performed to create a MEMS opening size of 300 × 200 μm and aluminum etching was performed under the opened window. The sensor structure was then defined by reactive ion etching (RIE) of the oxide, with the aluminum (Metal 2) layer serving as an etch stop. The aluminum layer was essential to precisely reduce the thickness of the microbridges to 2.52 μm and protect the polysilicon during the post-CMOS fabrication process, as illustrated in

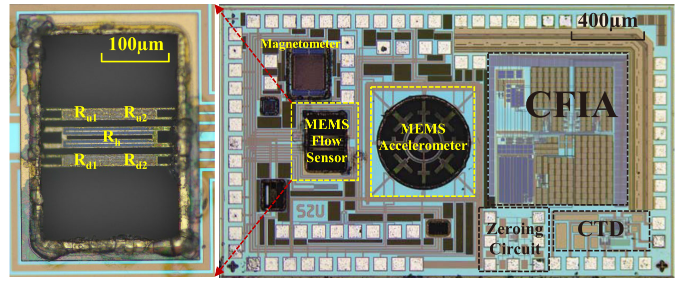

Fig. 8. Microphotograph of the fabricated SoC flow sensor using a SMIC 0.18 μm 1P6M CMOS-MEMS technology. Note the die size is 2.5 × 1.5 mm.

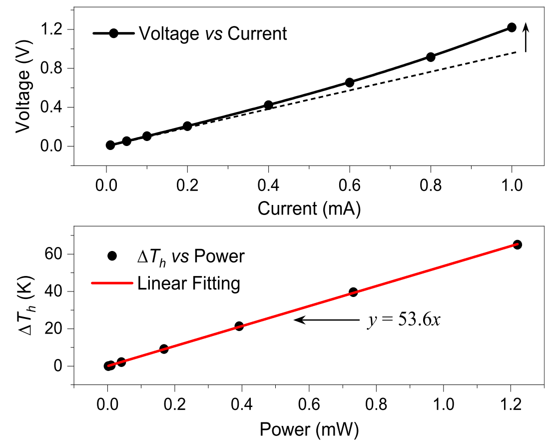

Fig. 9. (a) I–V characteristics of the microheater R_h. (b) Overheated temperature ΔT_h of the microheater at various power inputs.

Fig. 7(c). Deep RIE (DRIE) was then utilized to fabricate Si trenches with a depth of 80 μm, where the etch stop of the Al layer was removed in advance, as shown in Fig. 7(d) and (e). Finally, XeF_2 isotropic Si etching was employed to release the microbridges and increase the depth of the bottom cavity to about 100 μm, as shown in Fig. 7(f).

After removing the coated photoresist, the optical micrograph of the fabricated SoC flow sensor chip is shown in Fig. 8, where the MEMS sensor and interface circuits (including CFIA, the CTD control circuit, and the zeroing circuit) are monolithically integrated. Additionally, a multiaxis micro accelerometer and a MEMS magnetometer are implemented on the same die.

IV. Results and Discussion

Prior to assessing the performance of the SoC sensor, a preliminary evaluation of the MEMS sensor and its interface circuitry was conducted independently. For the MEMS sensor, the measured nonlinear I–V curve of the suspended microheater R_h proves that it experiences a significant temperature rise due to joule heating, as shown in Fig. 9(a). By using the known TCR, the resistance of the microheater ($R_h = V/I$) can be used to derive its overheated temperature ΔT_h. As shown in Fig. 9(b), a linear relationship between ΔT_h and input heating power is observed, while a prominent temperature rise of 53.6 K is obtained with an input heating power of less than 1 mW.

Fig. 10 shows the drive capability of the designed operational amplifier. When subjected to a load of 1.5 kΩ, the

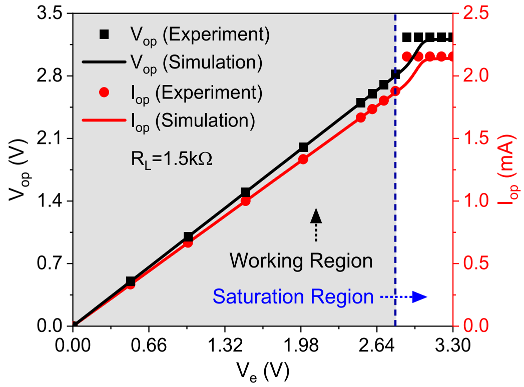

Fig. 10. With the configured load of 1.5 kΩ, the measured output swing and current drive capability of the op-amp are 2.82 V and 1.88 mA, which are consistent with the designed curve, and the variation of the working region range is less than 2.8%.

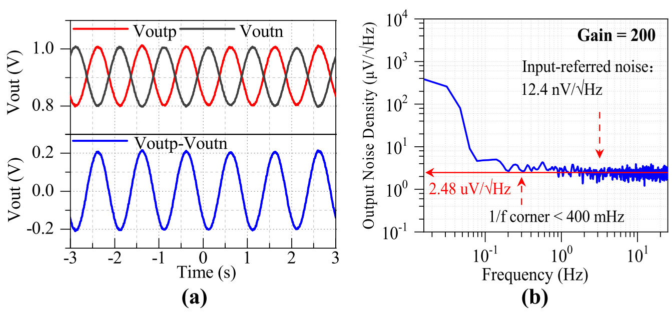

Fig. 11. (a) Measured output waveform of CFIA with a closed-loop gain of 200, where the 900 mV dc plus 1 mVpk sine ac signal is used as input. (b) Measured NSD of CFIA, where the input-referred noise floor is 12.4 nV/rtHz and the $1/f$ corner is less than 400 mHz.

output swing and current drive capability of the operational amplifier were measured as 2.82 V and 1.88 mA, respectively. Compared with the design results, the variation in the working region was found to be less than 2.8%.

Fig. 11(a) shows the transient results of the CFIA when the closed-loop gain is set as 200. For an input sinusoidal signal with a frequency of 1 Hz and a peak-to-peak value of 1 mV, the double-ended output V_{outp} and V_{outn} of the CFIA swing between 0.8 to 1 V at a common-mode voltage of 0.9 V, which leads to a differential output voltage with a sinusoidal peak-to-peak value of 200 mV. Fig. 11(b) shows the measured output NSD of the chopped CFIA from 15.625 mHz to 25 Hz, where the CFIA output is connected to a first-order passive differential *RC* filter with a cutoff frequency of 1 kHz. The flicker noise corner is significantly lower than 400 mHz, and the input-referred noise floor is 12.4 nV/$\sqrt{}$Hz. The discrepancy between the measured and simulated NSDs can be attributed primarily to the parasitic effects of layout design and CMOS process deviations. Furthermore, the linear output swing of the proposed CFIA is ±1.4 V, while considering the sensor interface circuit for respiration application within a low-frequency range (<4 Hz), the integrated output *rms* noise is 5.4 μVrms, which indicates that the CFIA has a dynamic range of 105 dB in such a scenario.

After completing the preliminary MEMS structure and circuit function test, the proposed SoC flow sensor was

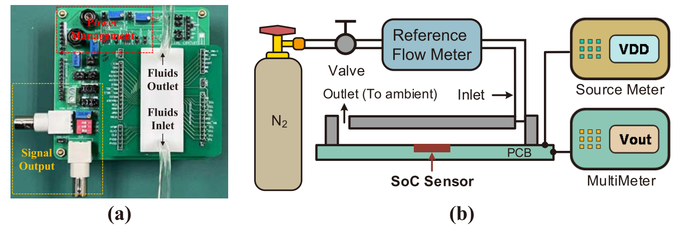

Fig. 12. (a) Packaged SoC flow sensor in a 3-D printed flow channel. (b) Experimental setup for the test of the SoC sensor with nitrogen gas flow.

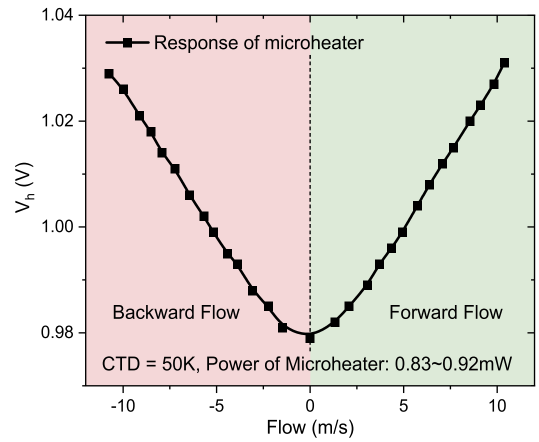

Fig. 13. Response of the CTD mode-based SoC flow sensor to an input N_2 gas flow of ±11 m/s. The single microheater shows an almost symmetric voltage output with a power consumption of 0.83–0.92 mW for the forward and backward gas flow.

then embedded in a PCB board and packaged in a 3-D printed flow channel with a size of 65 × 12 × 2.5 mm (Length × Width × Height), and tested with nitrogen gas flow at a room temperature of 26 °C, as illustrated in Fig. 12(a). The nitrogen tank was used as the gas source, and the pressure-reducing and throttle valves were employed to regulate the gas flow over the sensor chip. Meanwhile, a commercial flow sensor (AWM5104VN, Honeywell, USA) was used as a reference flowmeter, as shown in Fig. 12(b). In this case, the pressure difference observed between the inlet and outlet of the packaged SoC flow sensor was less than 1.6 kPa at the highest input gas flow. Notably, the entire SoC sensor system was powered by a single 3.3 V power supply, and the bandwidth of the whole system was limited to 4 Hz in the subsequent flow test.

Fig. 13 illustrates the voltage output of the microheater when subjected to an input N_2 gas flow ranging from −11 to 11 m/s in the CTD mode. Within this range, the power loss of the microheater is from 0.83 to 0.92 mW, while the power consumption of the entire CTD control circuit varies from 2.88 to 3.03 mW. Despite being a monotonic response to either forward or backward fluid flow, the voltage V_h across the microheater shows an almost symmetrical response to the bidirectional flow, which makes this voltage output unsuitable for measurements in the flow direction.

Fig. 14 shows the calorimetric output of the SoC sensor versus the input N_2 gas flow of ±11 m/s, and its response is monotonic for bidirectional flow. The SoC sensor exhibits a wide linear range of ±6 m/s, while a maximum sensitivity

TABLE I
PERFORMANCE COMPARISON OF PREVIOUS REPORTED CMOS-MEMS INTEGRATED FLOW SENSORS WITH OUR WORK

	[50]	[51]	[37]	[52]	[53]	[18]	[21]	**This work**
Sensor Principle	MEMS Thermal	MEMS Thermal	CMOS Thermal	MEMS Thermal	MEMS Thermal	MEMS Thermal	MEMS Coriolis	**MEMS Thermal**
Sensor Technology	2µm CMOS-MEMS	1µm SOI CMOS-MEMS	0.7µm CMOS	0.35µm CMOS-MEMS	2µm CMOS-MEMS	0.18µm CMOS-MEMS	MEMS	**0.18µm CMOS-MEMS**
Integration	Monolithic	Monolithic	Monolithic	Monolithic	Hybrid	Monolithic	Hybrid	**Monolithic**
Die Size (mm^2)	18	14.44	16	16	36	3	112.5[A] + 4.84[B]	**3.75**
ASIC Output	Digital	Analog	Digital	Analog	Analog	Analog	Digital	**Analog**
Fluids	Air	Air	Air	N_2	Air	Air	Gas & Liquid	**N_2**
Power (mW)	3[C]	9.4[D]	25[C]	4[D]	<452.6[D]	<30[C]; <1.72[D]	13[C]	**<4.96[C]; <0.92[D]**
Flow Range (m/s)	0.02 ~ 38 0.02 ~ 3[LR, @]	0~26	1 ~ 25	-3.33 ~ 3.33 -0.33 ~ 0.33[LR, @]	0.5 ~ 40	-15 ~ 15 -2 ~ 2[LR]	0 ~ 152.3[G] 0 ~ 0.49[L]	**-11 ~ 11 -6 ~ 6[LR]**
S^* (mV/(m/s)/mW)	N/A	0.94	N/A	2.3	3.93	288	N/A	**188**
MDFV (µm/s)	N/A	N/A	N/A	N/A	N/A	99	4.72×10^{4} [SD] 1.22×10^{3} [AD]	**309[SD] 86[AD]**

[A]MEMS die size, [B]CMOS die size; [C]Power of integrated sensor system; [D]Power of MEMS sensor; [G]Estimated gas flow velocity in MEMS channel; [L]Estimated liquid flow velocity in MEMS channel; [SD]Calculated by standard deviation; [AD]Calculated by Allan deviation; [LR]Linear range of MEMS thermal flow sensors; [@]Estimated from sensor output; N/A = Specification not available.

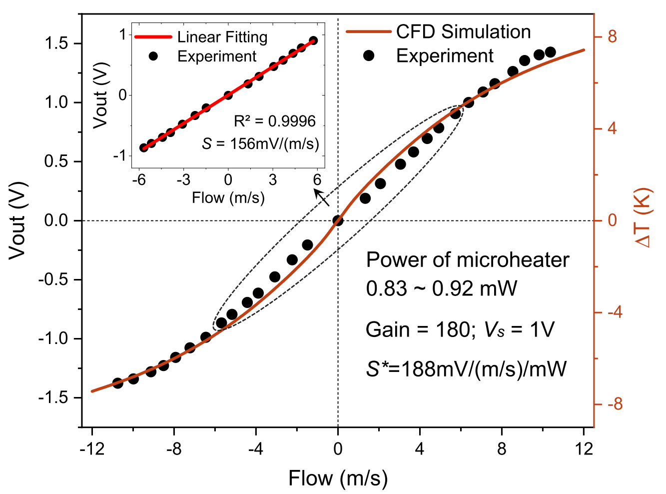

Fig. 14. Measured SoC sensor output as a function of input flow velocity ($\pm$11 m/s), and its comparison with the respective CFD simulation results. Note that the sensor has a good linear range of $\pm$6 m/s, with the normalized sensitivity S^* of 188 mV/(m/s)/mW.

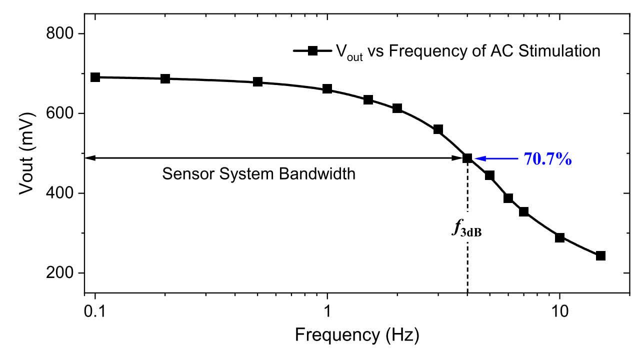

Fig. 15. Measured frequency response of the whole flow sensor system under an input gas flow of 4 m/s by ac sweeps on the microheater.

S of 156 mV/(m/s) is achieved in this linear flow region. Note that the sensitivity S is defined as the ratio of output V_{out} to the flow U. Additionally, the experiment achieved a relatively higher linear range of $\pm$6 m/s compared to the $\pm$4 m/s target in the CFD results. This enhancement is mainly attributed to the increased heat conduction of the aluminum traces at the supporting ends of the microbridges, which promotes a further reduction of the Pe number. Moreover, the normalized sensitivity S^* of the SoC sensor with respect to the microheater power is 188 mV/(m/s)/mW, which is better than the previously reported thermal flow sensors [51], [52], [53], while also achieving a 3$\times$ improvement in the linear range compared to [18], as shown in Table I.

In addition, the measurement shows that the CFIA consumes a power of 1.68 mW, and the Wheatstone bridge in the readout circuit has a power of around 0.25 mW. By adding the power of the CTD circuit, the whole SoC sensor system consumes a power of 4.81–4.96 mW within a flow of $\pm$11 m/s. Such an mW level power consumption is also much lower than the reported sensor system in Table I. Moreover, the predicted sensor output trend from the CFD model agrees well with the test results, demonstrating that both the CFD model and system-level model can be reliable and useful tools for further optimizing the CMOS-MEMS flow sensor system with a reduced footprint and power consumption.

Furthermore, the bandwidth of the whole SoC sensor system is approximately examined by subjecting the microheater to ac stimulation at different frequencies. Through the assessment of a sensor output attenuation of 70.7% at an input gas flow of 4 m/s, the bandwidth of the entire flow sensor system is successfully set to 4 Hz, as shown in Fig. 15.

In Fig. 16(a), a time diagram depicting the measured sensor signal over 10 000 s intervals with an acquisition rate of 40 samples/s is presented. The signal standard deviation σ of the SoC sensor is found to be 24.10 μV. By considering 95.4% of the population, the intrinsic minimum detectable flow velocity (MDFV $= 2\sigma/S$) and resolution ($Res. = 4\sigma/S$) of the whole SoC sensor system have been determined as 309 and 618 μm/s, respectively, as per [29], [36]. The MDFV and resolution could be further refined with the Allan deviation (specified in IEEE standard 1139-2008 [54]). Fig. 16(b) shows the minima of the Allan deviation, which is approximately

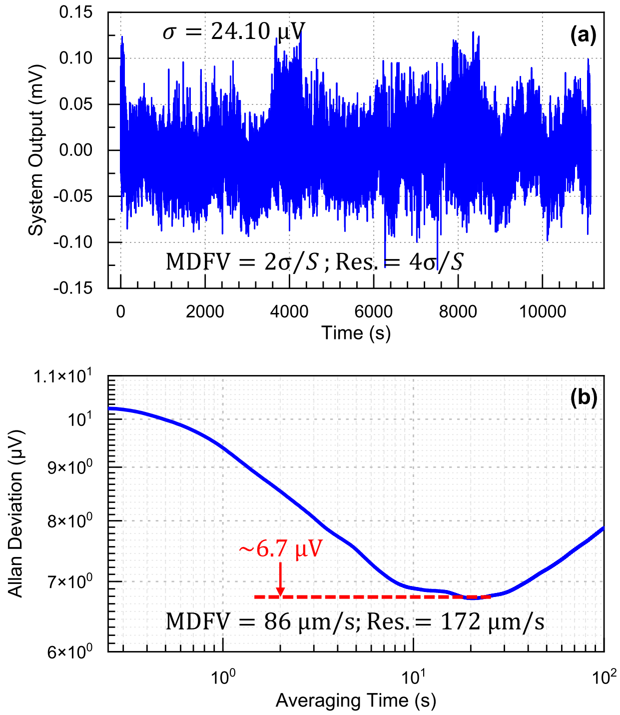

Fig. 16. (a) Long-term measured output of the SoC sensor at zero flow, the intrinsic MDFV of the sensor system is 309 μm/s. (b) Allan deviation of the flow output with the achieved lowest resolution of 172 μm/s.

6.7 μV. This indicates that by utilizing signal averaging, the SoC sensor can achieve a minimum MDFV of 86 μm/s and a resolution of 172 μm/s. These minima show competitive detection limits and resolution as compared with the state-of-the-art work in Table I.

V. Conclusion

To summarize, this article presented a CMOS-MEMS monolithic integrated thermal flow sensor system. The system comprises a MEMS sensor with dual pairs of thermistors, a precise CTD control circuit, and a low-noise readout circuit with a CFIA. The sensor's design and optimization are discussed in detail, along with its fabrication using an in-house developed post-CMOS process. The SoC sensor demonstrated high sensitivity, state-of-the-art linearity, and a detectable flow range down to 86 μm/s with a system power of less than 5 mW. Moreover, the results obtained from the SoC sensor are in good agreement with the theoretical models, validating the feasibility of the proposed design strategy. The developed SoC sensor holds significant promise for various applications in the field of flow sensing. Future work will investigate the temperature compensation scheme based on the system-level models, and seek the hardware solution for the low-cost (IoT) node in respiratory applications.

References

[1] F. Ejeian et al., "Design and applications of MEMS flow sensors: A review," *Sens. Actuators A, Phys.*, vol. 295, pp. 483–502, Aug. 2019.

[2] S. Silvestri and E. Schena, "Micromachined flow sensors in biomedical applications," *Micromachines*, vol. 3, no. 2, pp. 225–243, Mar. 2012.

[3] T. Dinh, T. Nguyen, H.-P. Phan, N.-T. Nguyen, D. V. Dao, and J. Bell, "Stretchable respiration sensors: Advanced designs and multifunctional platforms for wearable physiological monitoring," *Biosensors Bioelectron.*, vol. 166, Oct. 2020, Art. no. 112460.

[4] Z. Cao, R. Zhu, and R.-Y. Que, "A wireless portable system with microsensors for monitoring respiratory diseases," *IEEE Trans. Biomed. Eng.*, vol. 59, no. 11, pp. 3110–3116, Nov. 2012.

[5] T. Jiang et al., "Wearable breath monitoring via a hot-film/calorimetric airflow sensing system," *Biosensors Bioelectron.*, vol. 163, Sep. 2020, Art. no. 112288.

[6] X. Wang, Z. Ke, G. Liao, X. Pan, Y. Yang, and W. Xu, "A fast-response breathing monitoring system for human respiration disease detection," *IEEE Sensors J.*, vol. 22, no. 11, pp. 10411–10419, Jun. 2022.

[7] L. Huang et al., "A real-time wireless calorimetric flow sensor system with a wide linear range for low-cost respiratory monitoring," in *Proc. IEEE 36th Int. Conf. Micro Electro Mech. Syst. (MEMS)*, Munich, Germany, Jan. 2023, pp. 107–110.

[8] J. Wang, D. Xue, and X. Li, "Silicon monolithic microflow sensors: A review," *J. Micromech. Microeng.*, vol. 31, no. 10, Oct. 2021, Art. no. 104002.

[9] N. T. Nguyen, "Micromachined flow sensors—A review," *Flow Meas. Instrum.*, vol. 8, no. 1, pp. 7–16, Mar. 1997.

[10] J. T. W. Kuo, L. Yu, and E. Meng, "Micromachined thermal flow sensors—A review," *Micromachines*, vol. 3, no. 3, pp. 550–573, Jul. 2012.

[11] Z. Fang, X. Xu, L. Zhang, Y. Yang, and W. Xu, "An electrochemical impedance-based flexible flow sensor with ultra-low limit of detection," *IEEE Sensors J.*, vol. 22, no. 2, pp. 1180–1187, Jan. 2022.

[12] A. C. de Oliveira, J. Groenesteijn, R. J. Wiegerink, and K. A. A. Makinwa, "A MEMS coriolis mass flow sensor with 300 μg/h/$\sqrt{}$Hz resolution and $\pm$0.8 mg/h zero stability," in *IEEE Int. Solid-State Circuits Conf. (ISSCC) Dig. Tech. Papers*, Feb. 2021, pp. 84–86.

[13] S. C. C. Bailey et al., "Turbulence measurements using a nanoscale thermal anemometry probe," *J. Fluid Mech.*, vol. 663, pp. 160–179, Nov. 2010.

[14] M. Dijkstra, M. J. de Boer, J. W. Berenschot, T. S. J. Lammerink, R. J. Wiegerink, and M. Elwenspoek, "Miniaturized flow sensor with planar integrated sensor structures on semicircular surface channels," in *Proc. IEEE 20th Int. Conf. Micro Electro Mech. Syst. (MEMS)*, Jan. 2007, pp. 123–126.

[15] M. Dijkstra, T. S. J. Lammerink, M. J. de Boer, E. J. W. Berenschot, R. J. Wiegerink, and M. Elwenspoek, "Thermal flow-sensor drift reduction by thermopile voltage cancellation via power feedback control," *J. Microelectromech. Syst.*, vol. 23, no. 4, pp. 908–917, Aug. 2014.

[16] Z. Wang et al., "Analysis and compensation of benchmark drift of micromachined thermal wind sensor caused by packaging asymmetry," *IEEE Trans. Ind. Electron.*, vol. 69, no. 1, pp. 950–959, Jan. 2022.

[17] M. M. Sadeghi, R. L. Peterson, and K. Najafi, "Air flow sensing using micro-wire-bonded hair-like hot-wire anemometry," *J. Micromech. Microeng.*, vol. 23, no. 8, Aug. 2013, Art. no. 085017.

[18] W. Xu, X. Wang, Z. Ke, and Y.-K. Lee, "Bidirectional CMOS-MEMS airflow sensor with sub-mW power consumption and high sensitivity," *IEEE Trans. Ind. Electron.*, vol. 69, no. 3, pp. 3183–3192, Mar. 2022.

[19] Q. Zhang, W. Ruan, H. Wang, Y. Zhou, Z. Wang, and L. Liu, "A self-bended piezoresistive microcantilever flow sensor for low flow rate measurement," *Sens. Actuators A, Phys.*, vol. 158, no. 2, pp. 273–279, Mar. 2010.

[20] R. Zhang et al., "Nanogenerator as an active sensor for vortex capture and ambient wind-velocity detection," *Energy Environ. Sci.*, vol. 5, pp. 8528–8533, 2012.

[21] A. C. de Oliveira, S. Pan, R. J. Wiegerink, and K. A. A. Makinwa, "A MEMS coriolis-based mass-flow-to-digital converter for low flow rate sensing," *IEEE J. Solid-State Circuits*, vol. 57, no. 12, pp. 3681–3692, Dec. 2022.

[22] H. Wang et al., "Bioinspired fluffy fabric with in situ grown carbon nanotubes for ultrasensitive wearable airflow sensor," *Adv. Mater.*, vol. 32, no. 11, Mar. 2020, Art. no. 1908214.

[23] Z. Li, W. Chang, C. Gao, and Y. Hao, "A novel five-wire micro anemometer with 3D directionality for low speed air flow detection and acoustic particle velocity detecting capability," *J. Micromech. Microeng.*, vol. 28, no. 4, Apr. 2018, Art. no. 044004.

[24] Z. Liang, X. Guo, B. Yang, and T. Zhang, "Design and characterization of a novel biaxial bionic hair flow sensor based on resonant sensing," *Sensors*, vol. 20, no. 16, p. 4483, Aug. 2020.

[25] W. Xu, K. Song, S. Ma, B. Gao, Y. Chiu, and Y.-K. Lee, "Theoretical and experimental investigations of thermoresistive micro calorimetric flow sensors fabricated by CMOS MEMS technology," *J. Microelectromech. Syst.*, vol. 25, no. 5, pp. 954–962, Oct. 2016.

[26] W. Xu, M. Duan, M. Ahmed, S. Mohamad, A. Bermak, and Y.-K. Lee, "A low-cost micro BTU sensor system fabricated by CMOS MEMS technology," in *Proc. 19th Int. Conf. Solid-State Sensors, Actuators Microsyst.*, Jun. 2017, pp. 406–409.

[27] J. Wu, Y. Chae, C. P. L. van Vroonhoven, and K. A. A. Makinwa, "A 50 mW CMOS wind sensor with ±4% speed and ±2° direction error," in *IEEE Int. Solid-State Circuits Conf. (ISSCC) Dig. Tech. Papers*, Feb. 2011, pp. 106–108.

[28] W. Xu, X. Wang, X. Zhao, and Y.-K. Lee, "Two-dimensional CMOS MEMS thermal flow sensor with high sensitivity and improved accuracy," *J. Microelectromech. Syst.*, vol. 29, no. 2, pp. 248–254, Apr. 2020.

[29] W. Xu, X. Wang, X. Zhao, Z. Ke, and Y.-K. Lee, "An integrated CMOS MEMS gas flow sensor with detection limit towards micrometer per second," in *Proc. IEEE 33rd Int. Conf. Micro Electro Mech. Syst. (MEMS)*, Vancouver, BC, Canada, Jan. 2020, pp. 200–203.

[30] W. Fang et al., "CMOS MEMS: A key technology towards the 'more than Moore' era," in *Proc. 17th Int. Conf. Solid-State Sensors, Actuators Microsyst.*, Jun. 2013, pp. 2513–2518.

[31] H. Baltes, O. Paul, and O. Brand, "Micromachined thermally based CMOS microsensors," *Proc. IEEE*, vol. 86, no. 8, pp. 1660–1678, Aug. 1998.

[32] H. Qu, "CMOS MEMS fabrication technologies and devices," *Micromachines*, vol. 7, no. 1, p. 14, Jan. 2016.

[33] M. Ahmed, W. Xu, S. Mohamad, M. Duan, Y.-K. Lee, and A. Bermak, "Integrated CMOS-MEMS flow sensor with high sensitivity and large flow range," *IEEE Sensors J.*, vol. 17, no. 8, pp. 2318–2319, Apr. 2017.

[34] C. Hagleitner et al., "Smart single-chip gas sensor microsystem," *Nature*, vol. 414, no. 6861, pp. 293–296, Nov. 2001.

[35] C. Hagleitner, D. Lange, A. Hierlemann, O. Brand, and H. Baltes, "CMOS single-chip gas detection system comprising capacitive, calorimetric and mass-sensitive microsensors," *IEEE J. Solid-State Circuits*, vol. 37, no. 12, pp. 1867–1878, Dec. 2002.

[36] P. Bruschi and M. Piotto, "Design issues for low power integrated thermal flow sensors with ultra-wide dynamic range and low insertion loss," *Micromachines*, vol. 3, no. 2, pp. 295–314, Apr. 2012.

[37] W. Brevet, F. Sebastiano, and K. Makinwa, "A 25 mW smart CMOS wind sensor with corner heaters," in *Proc. 41st Annu. Conf. IEEE Ind. Electron. Soc.*, Nov. 2015, pp. 1194–1199.

[38] A. De Luca and F. Udrea, "CMOS MEMS hot-film thermoelectronic flow sensor," *IEEE Sensors Lett.*, vol. 1, no. 6, pp. 1–4, Dec. 2017.

[39] W. Xu, B. Wang, M. Duan, M. Ahmed, A. Bermak, and Y.-K. Lee, "A three-dimensional integrated micro calorimetric flow sensor in CMOS MEMS technology," *IEEE Sensors Lett.*, vol. 3, no. 2, pp. 1–4, Feb. 2019.

[40] T.-W. Shen, K.-C. Chang, C.-M. Sun, and W. Fang, "Performance enhance of CMOS-MEMS thermoelectric infrared sensor by using sensing material and structure design," *J. Micromech. Microeng.*, vol. 29, no. 2, Feb. 2019, Art. no. 025007.

[41] W. Xu, X. Wang, R. Wang, J. Xu, and Y.-K. Lee, "CMOS MEMS thermal flow sensor with enhanced sensitivity for heating, ventilation, and air conditioning application," *IEEE Trans. Ind. Electron.*, vol. 68, no. 5, pp. 4468–4476, May 2021.

[42] M. Elwenspoek and R. Wiegerink, *Mechanical Microsensors*. Cham, Switzerland: Springer, 2012.

[43] W. Xu, S. Ma, X. Wang, Y. Chiu, and Y.-K. Lee, "A CMOS-MEMS thermoresistive micro calorimetric flow sensor with temperature compensation," *J. Microelectromech. Syst.*, vol. 28, no. 5, pp. 841–849, Oct. 2019.

[44] Z. Li et al., "System-level modeling and design of a temperature compensated CMOS MEMS thermal flow sensor," in *Proc. IEEE Int. Symp. Circuits Syst. (ISCAS)*, Austin, TX, USA, May 2022, pp. 2072–2076.

[45] B. Li, W. Xu, M. Paszkiewicz, Z. Li, R. Wang, and Y. K. Lee, "Theoretical and experimental study of Peclet number effect on the linearity of thermoresistive micro calorimetric flow sensors," in *Proc. APCOT Conf.*, 2018, pp. 1–3.

[46] R. Wu, K. A. A. Makinwa, and J. H. Huijsing, "A chopper current feedback instrumentation amplifier with a 1 mHz 1/f noise corner and an AC-coupled ripple reduction loop," *IEEE J. Solid-State Circuits*, vol. 44, no. 12, pp. 3232–3243, May 2009.

[47] E. Sackinger and W. Guggenbuhl, "A versatile building block: The CMOS differential difference amplifier," *IEEE J. Solid-State Circuits*, vol. SSC-22, no. 2, pp. 287–294, Apr. 1987.

[48] M. Ahmed, W. Xu, S. Mohamad, F. Boussaid, Y.-K. Lee, and A. Bermak, "Fully integrated bidirectional CMOS-MEMS flow sensor with low power pulse operation," *IEEE Sensors J.*, vol. 19, no. 9, pp. 3415–3424, May 2019.

[49] S. O. Cannizzaro, A. D. Grasso, R. Mita, G. Palumbo, and S. Pennisi, "Design procedures for three-stage CMOS OTAs with nested-Miller compensation," *IEEE Trans. Circuits Syst. I, Reg. Papers*, vol. 54, no. 5, pp. 933–940, May 2007.

[50] F. Mayer, A. Haberli, H. Jacobs, G. Ofner, O. Paul, and H. Baltes, "Single-chip CMOS anemometer," in *IEDM Tech. Dig.*, Washington, DC, USA, Mar. 1997, pp. 895–898.

[51] M. Mansoor et al., "An SOI CMOS-based multi-sensor MEMS chip for fluidic applications," *Sensors*, vol. 16, no. 11, p. 1608, Nov. 2016.

[52] P. Bruschi, M. Dei, and M. Piotto, "A single chip, double channel thermal flow meter," *Microsyst. Technol.*, vol. 15, no. 8, pp. 1179–1186, Aug. 2009.

[53] Z. Dong, J. Chen, Y. Qin, M. Qin, and Q.-A. Huang, "Fabrication of a micromachined two-dimensional wind sensor by Au–Au wafer bonding technology," *J. Microelectromech. Syst.*, vol. 21, no. 2, pp. 467–475, Apr. 2012.

[54] *IEEE Standard Definitions of Physical Quantities for Fundamental Frequency and Time Metrology—Random Instabilities*, IEEE Standard 1139-2008, 2009.

Wei Xu (Senior Member, IEEE) received the B.S. and M.S. degrees from the Huazhong University of Science and Technology, Wuhan, China, in 2010 and 2013, respectively, and the Ph.D. degree from the Hong Kong University of Science and Technology, Hong Kong, in 2017.

He is currently an Associate Professor with the College of Electronics and Information Engineering, Shenzhen University, Shenzhen, China. He has published more than 60 articles in reputed international journals and conferences, such as IEEE/ASME JOURNAL OF MICROELECTROMECHANICAL SYSTEMS, *Journal of Micromechanics and Microengineering*, IEEE TRANSACTIONS ON INDUSTRIAL ELECTRONICS, IEEE TRANSACTIONS ON INSTRUMENTATION AND MEASUREMENT, IEEE SENSORS JOURNAL, Proc. of IEEE MEMS, IEEE TRANSDUCERS, and IEEE SENSORS. His research interest focuses on CMOS-MEMS sensors.

Dr. Xu was a corresponding author of the Outstanding Student Paper Award from the IEEE MEMS 2020 in Vancouver, BC, Canada. He has also served as a Technical Committee Member for the IEEE Circuits and Systems Society (CASS) on Sensory Systems.

Zhijuan Li received the M.S. degree in electronic science and technology from Shenzhen University, Shenzhen, China.

Her research interests include analog mixed-signal circuits, sensor interfaces, and integrated microsystems.

Zetao Fang received the B.S. and M.S. degrees in electronic science and technology from Shenzhen University, Shenzhen, China.

His research interests include analog circuits, sensor interfaces, and CMOS MEMS design.

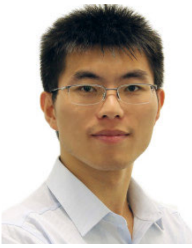

Bo Wang (Senior Member, IEEE) received the B.Eng. degree (Hons.) in electrical engineering from Zhejiang University, Hangzhou, China, in 2010, and the M.Phil. and Ph.D. degrees in electronic and computer engineering from The Hong Kong University of Science and Technology (HKUST), Hong Kong, in 2012 and 2015, respectively.

In 2015, he joined HKUST as a Post-Doctoral Researcher and led the HKUST-MIT Consortium project on wireless sensing node design for smart green building applications. He has been with the Massachusetts Institute of Technology, Cambridge, MA, USA, as a Visiting Scientist since 2016. In 2017, he joined Hamad Bin Khalifa University, Doha, Qatar, as a Founding Faculty and an Assistant Professor, where he is currently an Associate Professor with the Division of Information and Computing Technology, College of Science and Engineering. His research interests include energy-efficient analog mixed-signal circuits, sensor and sensor interfaces, and heterogeneous integrated systems for in vitro/vivo health monitoring.

Dr. Wang was a recipient of the IEEE ASP-DAC Best Design Award in 2016. He serves as a Technical Committee Member of the IEEE CAS Committee on sensory systems. He is an Associate Editor of the IEEE Sensors Journal.

Linze Hong received the B.S. degree in microelectronics from Shenzhen University, Shenzhen, China, where he is currently pursuing the master's degree in integrated circuit engineering.

His research interests include CMOS MEMS sensors, wearable devices, and mathematical modeling.

Gai Yang is currently pursuing the master's degree with the Beijing Institute of Technology, Beijing, China.

His current research interests include SAW humidity sensors and CMOS-MEMS humidity sensors.

Su-Ting Han received the Ph.D. degree in physics and materials science from the City University of Hong Kong, Hong Kong SAR, in 2014.

From 2014 to 2016, she was a Post-Doctoral Research Fellow at the City University of Hong Kong. She joined Shenzhen University in 2016 as an Associate Professor (tenure track) and was promoted to Full Professor (tenured) in 2021 and then Distinguished Professor in 2022. She was a Visiting Professor at the Department of Electrical Engineering and Computer Science at the University of Michigan, USA, in 2019. Her research interests include flash memory, memristor, neuromorphic computing, and in-memory computing systems.

Xiaojin Zhao (Senior Member, IEEE) received the B.Sc. degrees in both microelectronics and applied mathematics from Peking University, Beijing, China, in 2005, and the Ph.D. degree in electrical and electronic engineering from The Hong Kong University of Science and Technology (HKUST), Hong Kong, China, in 2010.

From 2010 to 2011, he was a Post-Doctoral Research Associate with HKUST. In 2012, he joined Shenzhen University, Shenzhen, China, where he is currently a Full Professor with the State Key Laboratory of Radio Frequency Heterogeneous Integration and the College of Electronics and Information Engineering. In 2014, he was a Visiting Scholar with IMEC, Leuven, Belgium. He has published 113 international journal articles and peer-reviewed conference papers (mostly in IEEE). His research interests include CMOS/MEMS monolithic image sensor, gas sensor, and their related hardware security techniques (e.g., physical unclonable function and true random number generator) when applied to the field of smart Internet of Things (IoT).

Dr. Zhao serves as an Associate Editor for IEEE Sensors Journal and has served as an organizing/technical committee member in various IEEE conferences (e.g., DAC, ISCAS, APCCAS, and AsianHOST). He also serves as a Technical Committee Member for the IEEE Circuits and Systems Society (CASS) on Sensory Systems and the IEEE Circuits and Systems Society (CASS) on VLSI Systems and Applications. He was a co-recipient of the Best Student Paper Award from the IEEE EDSSC'2018 in Shenzhen, China, and the Outstanding Student Paper Award from the IEEE MEMS'2020 in Vancouver, BC, Canada. He has one paper selected as the cover page of the IEEE Electron Device Letters (EDL) in 2020 and two papers selected as the finalist of the Best Paper Award for AsianHOST'2017 in Beijing, and AsianHOST'2019 in Xi'an, China. He has served as the Vice Chair and the Chair for the IEEE Electron Devices and Solid-State Circuits (EDSSC) Shenzhen Joint Chapter from 2015 to 2019. He also serves as the Chair for the IEEE Circuits and Systems (CAS) Shenzhen Chapter.

Xiaoyi Wang (Member, IEEE) is currently an Associate Professor with the School of Integrated Circuits and Electronics, Beijing Institute of Technology, Beijing, China. He has published more than 50 international journal and conference papers, including IEEE Transactions on Industrial Electronics, *Journal of Microelectromechanical Systems*, IEEE Transactions on Instrumentation and Measurement, IEEE Transactions on Electron Devices, *Microsystems and Nanoengineering*, *ACS Applied Materials & Interfaces*, IEEE MEMS Conference, and Transducers. His research interests mainly focus on the CMOS-MEMS monolithic integrated artificial intelligent sensors equipped with artificial intelligence (AI) technology for physical/chemical information sensing, storage, process, and analysis including structural health monitoring sensors, environmental sensing hubs, gas sensor arrays, and electric power sensing units. He also focuses on micro/nanofabrication technology, soft electronics, integrated microsystems, and their applications in industries, smart homes, and healthcare.